JOURNAL OF GEOPHYSICAL RESEARCH, VOL. 107, NO. C8, 3106, 10.1029/2001JC000837, 2002

Spaceborne synthetic aperture radar observations of ocean waves traveling into sea ice

Johannes Schulz-Stellenfleth and Susanne Lehner
German Aerospace Center, Remote Sensing Technology Institute, Oberpfaffenhofen, Germany

Received 12 February 2001; revised 10 September 2001; accepted 27 November 2001; published 15 August 2002.

[1] Damping of ocean waves by sea ice is studied using spaceborne synthetic aperture radar (SAR) images of the marginal ice zone (MIZ) acquired by the European Remote sensing satellite ERS-2. SAR imaging of waves damped by sea ice is analyzed theoretically. The impact of sea ice on the azimuthal cutoff is studied by simulation of the azimuthal SAR image autocorrelation function as well as the two- dimensional SAR image spectrum. Typical imaging artifacts like spiky wave crests and wave refraction seen on SAR scenes of the MIZ are reproduced by simulation. Sensitivity studies are performed using models for wind sea and swell systems. It is shown that the degradation of the azimuthal SAR image resolution is dominated by the orbital velocity variance of the waves, while the coherence time of the complex radar reflectivity has a minor impact. A first-order analysis of wave damping observed on SAR scenes is carried out using a technique that was originally developed for wind estimation by *Kerbaol et al.* [1998]. The method does not require a priori information and is insensitive to real aperture modulation. The azimuthal SAR image cutoff wavelength is estimated and related to the orbital velocity variance of the sea surface by regression. The model is fitted on the basis of a global set of model ocean wave spectra. The technique is applied within the sea ice and in the open water in front of the ice boundary. On the basis of simple models for wind sea and swell, ocean wave attenuation rates are obtained from the observed orbital velocity decrease of waves entering the ice. The required wind information is derived from calibrated SAR data using the CMOD method. Two case studies showing examples from the Greenland and the Weddell Seas are given. It is shown that the estimated wave damping is consistent with damping parameters found in earlier field campaigns carried out in the Weddell Sea and the Bering Sea. An inversion technique providing estimates for the two-dimensional wave spectra behind and in front of the ice boundary as well as a two-dimensional filter function characterizing the sea ice impact is introduced. The technique is based on simultaneous inversion of the two-dimensional image spectra in the open water and within the ice using a priori information from an ocean wave model. It is shown that the technique gives results consistent with the first-order analysis based on the cutoff estimation. *INDEX TERMS:* 4540 Oceanography: Physical: Ice mechanics and air/sea/ice exchange processes; 4560 Oceanography: Physical: Surface waves and tides (1255); 4594 Oceanography: Physical: Instruments and techniques; *KEYWORDS:* sea ice, synthetic aperture radar, ocean waves

1. Introduction

[2] Sea ice covers an area which encompasses about two thirds of the permanent global ice cover. Sea ice is an important factor in the climate system [*Hartmann*, 1994; *Wadhams*, 2000] as it has a strong impact on the albedo, the atmosphere-ocean heat and momentum exchange, and the oceanic salt flux. It plays an important role in shipping and offshore operations in the polar regions as well [*Johannessen et al.*, 1995].

[3] Sea ice responds sensitively to small changes of the oceanic or atmospheric conditions and is therefore a valuable indicator for climate change [*Wadhams*, 2000]. Therefore, continuous measurements of sea ice parameters like ice thickness and ice concentration is an urgent need for scientists as well as for mariners.

[4] The present work is concerned with remote sensing of sea ice in the marginal ice zone (MIZ), which is the transition zone between open water and pack ice. Because of the tough environmental conditions in the MIZ remote sensing is so far the only way to obtain sea ice information on a continuous basis. Due to their all weather capability microwave sensors like synthetic aperture radar (SAR) or the radiometer play an important role in this context. Radiometric systems like the Special Sensor Microwave Imager (SSM/I) [*Bjorgo et al.*, 1997] with a resolution between 10 and 50 km (depending on frequency) are mainly

0148-0227/02/2001JC000837$09.00

used to measure sea ice coverage and sea ice type. SAR imagery as acquired by the European Remote Sensing Satellite (ERS) has a resolution of about 20 m and thus allows to study processes in the MIZ on a smaller scale.

[5] In this study ERS SAR scenes acquired in the Greenland Sea and the Weddell Sea are used to analyse the damping of ocean waves traveling into the MIZ by sea ice. The analysis of ocean waves entering sea ice has two facets: the physical effects of waves on an ice cover or vice versa; and the use of waves as a diagnostic tool in ice mechanics. In this study ERS SAR data will be used to study the second aspect which is the impact of sea ice on the two-dimensional ocean wave spectrum.

[6] SAR observations of ocean waves in sea ice have been analyzed in several studies [*Vachon et al.*, 1993; *Lyzenga et al.*, 1985; *Wadhams and Holt*, 1991; *Liu et al.*, 1991a, 1991b] some of them discussing methods to estimate ice parameters [*Shuchman and Rufenach*, 1994]. Different models were proposed to explain phenomena like wave refraction at the ice edge. Whereas some studies consider hydrodynamic ocean wave sea ice interaction alone [*Shuchman and Rufenach*, 1994] others also discuss SAR imaging artifacts [*Vachon et al.*, 1993].

[7] In the present study several new techniques based on complex SAR data, which have been originally developed to measure ocean waves in the open water, are applied to ocean waves in the MIZ. The main idea is to use the fact that SAR is sensitive to the movement of imaged targets (train off the track effect). SAR can thus be used to measure sea surface motion and in particular the change of motion when waves enter a sea ice region. A technique originally developed by *Kerbaol et al.* [1998] for wind measurements is applied to estimate the orbital velocity variance of the sea surface. The technique is insensitive to the real aperture radar (RAR) modulation and is therefore ideally suited for sea ice where the detailed RAR mechanism is in general not known.

[8] The impact of a possible increase of the coherence time within sea ice as discussed by *Vachon et al.* [1993] for airborne data is analyzed. It is shown that for the ERS SAR configuration the degraded azimuthal resolution is dominated by the orbital velocity variance, while coherence time has a minor impact. The azimuthal cutoff wavelength can therefore be used to gain information about the orbital sea surface motion in the open water as well as in sea ice.

[9] The estimated degraded resolution is related to the orbital velocity variance of the sea surface by fitting a linear model. The fit procedure is based on a global data set of wave model spectra provided by the European Centre for Medium-Range Weather Forecasts (ECMWF). The azimuthal SAR image autocorrelation function is simulated using a nonlinear forward model. Orbital velocity contributions from wavelength down to the backscattering facet size are taken into account.

[10] Sensitivity studies for the orbital velocity variance are carried out using simplified models for wind sea and swell. It is shown that the cutoff wavelength in front of the ice edge strongly depends on the local wind field, while swell has a minor impact.

[11] Applying the cutoff estimation technique orbital velocities are estimated behind and in front of the ice boundary using ERS SAR scenes acquired over the Weddell and the Greenland Sea. To separate the orbital velocity contributions from swell and wind sea the CMOD method, which estimates the wind speed from calibrated SAR data, is applied. It is shown that the reduction of the orbital velocity variance measured by SAR is consistent with earlier field campaign measurements reported by *Wadhams et al.* [1988].

[12] In the last section a new inversion technique which gives detailed information on the two-dimensional wave spectra before and behind the ice boundary using prior information from a wave model is presented. The method provides a two-dimensional filter function which characterizes the sea ice impact on the ocean wave spectrum. It is shown that although the method uses wave model spectra and needs information on the RAR modulation within the sea ice, it gives results consistent with the cutoff estimation technique, which is independent of both RAR modulation and a priori information.

2. Ocean Wave Attenuation by Sea Ice

[13] The attenuation of ocean waves by sea ice is a well known effect [*Squire et al.*, 1995]. *Wadhams et al.* [1988] reports about in situ wave measurements carried out in the Greenland and Bering Sea. The experiments suggest that the wave energy decay is approximately negative exponential with increasing distance γ from the ice boundary. For a given wave number k with wave energy $F_k(0)$ in the open water the wave energy within the sea ice is thus given by

$$F_k(\gamma) = F_k(0)\exp(-\rho\,\gamma) \tag{1}$$

with damping rate ρ. Damping rates for different wavelength reported by *Wadhams et al.* [1988] are shown in Figure 1. Frequency was converted into wavelength using the dispersion relation for deep water. The highest frequency measured is about 0.2 Hz which corresponds to about 40 m wavelength. Damping rate estimates were obtained under various ice conditions in the Greenland Sea and the Bering Sea. As can be seen the damping rate has a high variability especially for shorter waves. The experiments showed that the damping rates increase with decreasing wavelength except for some rollover effects which were observed at the shortest wavelength in some cases. The e-folding distance for a 100 m wave goes down to 1–2 km in some cases, while it is well over 20 km for most wave systems longer than 250 m.

[14] Due to the complex mechanical properties of sea ice wave damping is still not fully understood theoretically [*Squire et al.*, 1995]. A simple model which is appropriate for frazil, brash and pancake ice describes sea ice as a viscous layer of constant thickness h and ice concentration c is the mass load model [*Wadhams et al.*, 1988]. The model predicts a slightly modified dispersion relation resulting in a reduced phase speed within the ice. It follows that there exists a critical wave frequency ω_c beyond waves are totally reflected at the ice boundary.

$$\omega_c = \sqrt{\frac{\rho_W\, g}{\rho_I\, c\, h}} \tag{2}$$

Here $\rho_I \approx 900$ kg m^{-3} and $\rho_W \approx 1025$ kg m^{-3} are the densities of ice and water respectively. Cutoff wavelength for a given

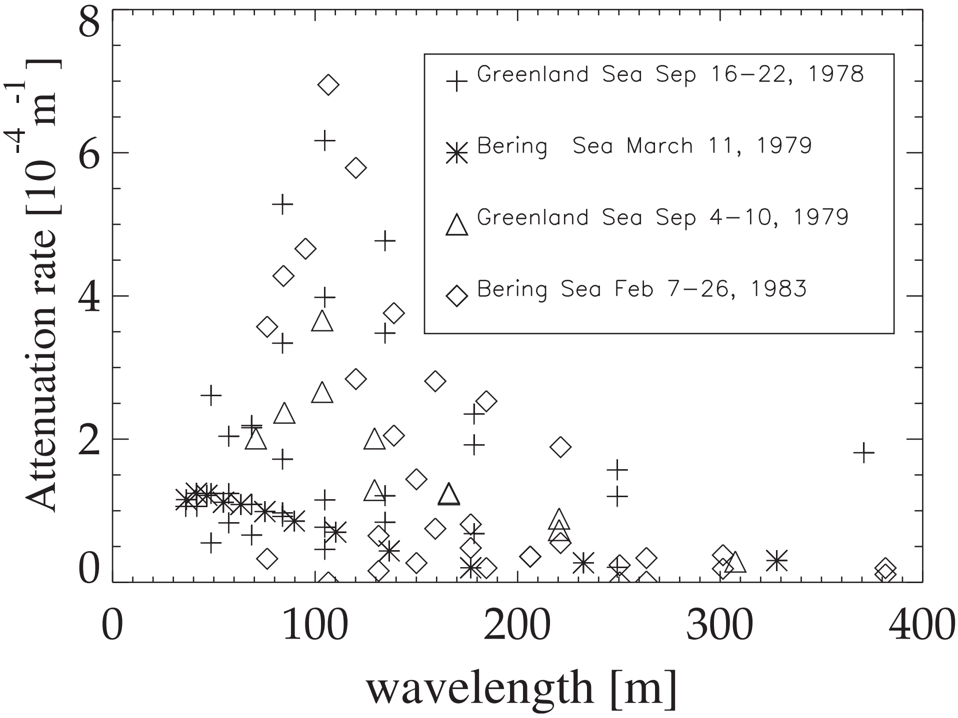

Figure 1. Attenuation rates of ocean waves damped by sea ice as reported by *Wadhams et al.* [1988] (compare equation (1)). The estimates were obtained under various ice conditions in the Greenland Sea and the Bering Sea.

product of c and h are shown in Figure 2. The indicated intervals for $c\ h$ are typical for frazil and brash ice. It can be seen that under realistic sea ice conditions only waves shorter than about 25 m are totally reflected at the ice boundary.

[15] Another feature of the mass load model is the refraction of waves towards the normal of the ice boundary. Denoting the incidence angle with α, the angle of refraction with β and the wave number in the open water with k_W the following refraction law follows:

$$\frac{\sin\beta}{\sin\alpha} = \frac{k_W}{k_I} \tag{3}$$

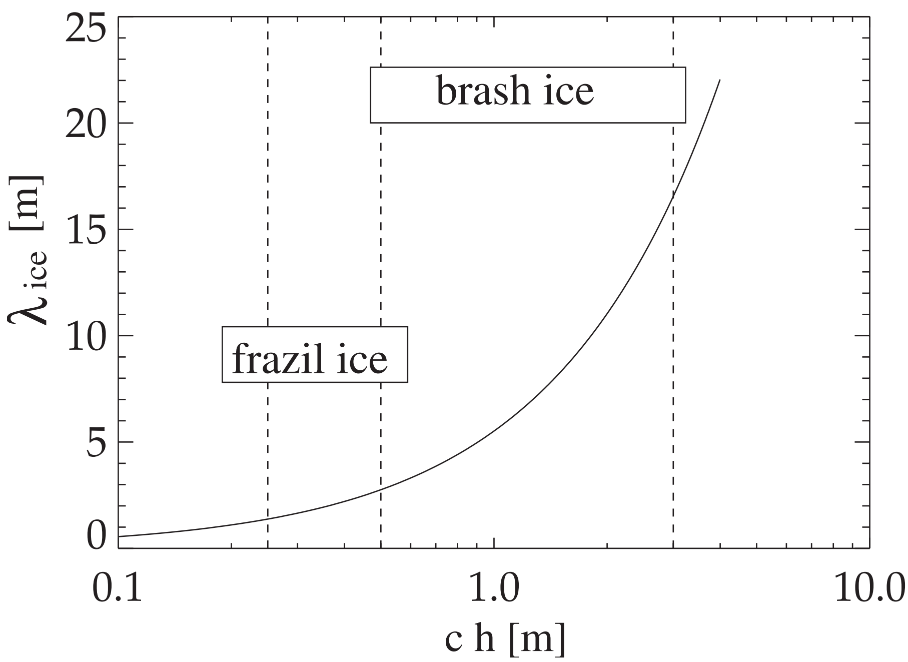

Figure 2. Cutoff wavelength as predicted by the mass load model (compare equation (2)) depending on the product of ice thickness h and ice concentration c.

The wave number k_I of the refracted wave in the sea ice is given by the following expression:

$$k_I = \frac{k_W}{1 - c\, h\, k_W\, \rho_I/\rho_W} \tag{4}$$

[16] The mass load model is not able to reproduce the observed continuous energy decay of waves entering an ice region with individual ice floes. This problem is more complicated because it crucially depends on the size, distribution and mechanical properties of the ice floes. Several models exist describing the process. A model reproducing in situ measurements quite well except for the observed rollover effect is the multiple scattering model [*Wadhams et al.*, 1988].

3. SAR Ocean Wave Imaging Theory

[17] As the SAR imaging mechanism is sensitive to both the radar cross section and the motion of the sea surface, it is a complex process. Models describing this mechanism and inversion schemes for the SAR retrieval of two-dimensional ocean wave spectra have been developed [*Alpers et al.*, 1981; *Lyzenga*, 1988; *Hasselmann and Hasselmann*, 1991; *Mastenbroek and de Valk*, 2000; *Hasselmann et al.*, 1996; *Engen and Johnson*, 1995; *Krogstad et al.*, 1994].

[18] In this section the main features of the common theory for SAR ocean wave imaging in open water is recaptured and the impact of sea ice on the imaging process is discussed. The model consists of three main parts. First of all the local radar backscattering mechanism is explained. After discussing the modulation of the local backscatter processes by long waves (longer than twice the SAR resolution cell) the impact of sea surface motion on the SAR image formation is explained. The impact of sea ice on each part of the model is discussed.

3.1. Backscattering Model

[19] According to common theory microwave radar backscatter from the ocean surface is dominated by Bragg scattering for incidence angles between 20° and 60° [*Hasselmann et al.*, 1985]. The backscatter is thus dependent on the sea surface roughness at the scale of the radar wavelength, which is about 5 cm for the ERS SAR. With incidence angles between 20° and 26° ERS SAR imaging falls into the Bragg regime.

[20] The radar return from sea ice is more complicated as different backscattering mechanisms are involved. The radar cross section is a combination of surface and volume scattering and heavily depends on the detailed history of the sea ice. For first year ice surface scattering dominates. For multiyear ice volume scattering from air bubbles has to be taken into account. Details about the backscattering process are not essential for the present study and are therefore not discussed further.

[21] To model the SAR imaging process in the open water as well as in the sea ice the spatial and temporal correlation properties of the complex reflectivity r have to be known. As in most studies we will assume that r is a spatially white process. For the temporal correlation of r in the open water we assume a coherence time τ_s of about 50 ms for C band [*Carande*, 1994]. There is some indication that the coherence time for sea ice is longer than for open water [*Vachon et al.*, 1993]. However, it will be shown that it is not necessary to quantify this increase in detail for the present study. For both open water and sea ice the autocorrelation of r is thus given as follows.

$$\langle r(\mathbf{x_1}, t_1) r^*(\mathbf{x_2}, t_2) \rangle = \sigma\left(\mathbf{x_1}, \frac{t_1 + t_2}{2}\right) \delta(\mathbf{x_1} - \mathbf{x_2}) \exp\left(-\frac{(t_1 - t_2)^2}{\tau_s^2}\right) \tag{5}$$

Here σ is the normalized radar cross section (NRCS).

[22] Based on the previous assumptions SAR ocean wave imaging in the open ocean can be explained by a two scale model, which divides the sea surface into two spatial scales separated by a wave number k_{sep}. The separation wave number can be chosen either independent of the SAR sensor from pure electrodynamic hydrodynamic considerations (EMH model) [*Hasselmann et al.*, 1985] or dependent on the SAR resolution (SAR two scale model) [*Hasselmann et al.*, 1985; *Kasilingam and Shemdin*, 1990]. In this study the EMH model is used, which is based on the backscatter from single facets consisting of a small number (about 10) of Bragg wavelength. For the ERS SAR the facette size is thus on the order of 0.5 m.

[23] The choice of model has some implications for the interpretation of the coherence time τ_s defined in equation (5). Within the SAR two scale model τ_s refers to the temporal decorrelation of the backscatter returned from a SAR resolution cell, which is an order of magnitude larger than a facet, at least for the ERS SAR system with about 20 m resolution. As this decorrelation does not only depend on the time evolution of the small scale facets (intrinsic decorrelation) but also on the motion of the intermediate waves shorter than twice the SAR resolution and longer than the facet size, the corresponding coherence time is shorter [*Vachon et al.*, 1993].

3.2. Real Aperture Modulation

[24] It is assumed that long ocean waves (longer than twice the SAR resolution) are imaged by the modulation of the local backscattering process taking place at the short length scale. Neglecting motion effects the imaging mechanism is dominated by real aperture radar (RAR) modulation, e.g. long ocean waves modulate the radar cross section by geometric (tilt modulation, range-bunching) and hydrodynamic (hydrodynamic modulation) mechanisms. RAR modulation dominates imaging of range traveling (perpendicular to flight direction) waves and is in general assumed to be a linear process [*Alpers et al.*, 1981]. It can therefore be described using a transfer function T^{RAR}. As all three modulation mechanisms are assumed to be independent T^{RAR} can be expressed as the sum of the respective transfer functions.

$$T^{RAR} = T^{tilt} + T^{hydr} + T^{rb} \tag{6}$$

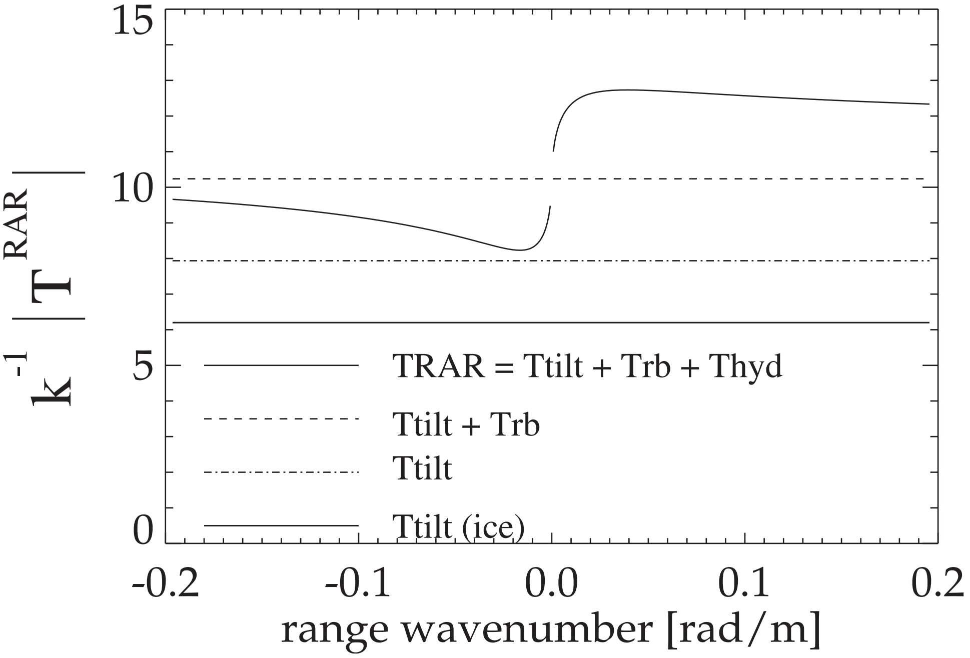

Figure 3. Modulus (A) of (normalized) tilt, range bunching, and hydrodynamic modulation transfer functions. VV polarization and 23° incidence angle are assumed. The tilt transfer function for ice was derived by extrapolating measurements reported by *Vachon and Krogstad* [1994].

For vertical polarization in transmit and receive (VV) and a right looking SAR analytical expressions for the transfer functions are given by

$$T_k^{tilt} = -\frac{4\,i\,k_y\,\cot\theta}{1+\sin^2\theta} \tag{7}$$

$$T_k^{rb} = -i\,k_y\,\frac{\cos\theta}{\sin\theta} \tag{8}$$

$$T_k^{hyd} = 4.5\,\omega\,\frac{k_y^2}{|k|}\,\frac{\omega - i\mu}{\omega^2+\mu^2} \tag{9}$$

Here θ is the incidence angle and μ is the hydrodynamic relaxation rate which was set to 0.5 s^{-1} in the open water [*Hasselmann and Hasselmann*, 1991].

[25] Figure 3 shows the modulus (A) and phase (B) of the normalized MTF T^{RAR}/k_y for 23° incidence angle and VV polarization. The solid line represents the theoretical RAR MTF, while the dashed and dashed dotted lines refer to tilt MTF and range bunching MTF respectively.

[26] The lower dashed dot dotted line in Figure 3 was calculated by extrapolating airborne tilt MTF measurements over ice performed by *Vachon et al.* [1993]. For incidence angles between 40° and 75° and VV polarization the following tilt MTF was derived

$$\overline{T_k^{tilt}} = i\,k_y\,\frac{180\,log(10)}{10\,\pi}(2A\,\theta + B) \tag{10}$$

with A = 0.0022, B = −0.56, and θ given in degree. As the estimation of the tilt MTF for 20° incidence angle by extrapolation is unlikely to give accurate results and the obtained value is only 20% different from the theoretical value for the open sea we will use the theoretical tilt MTF for both open water and sea ice. Hydrodynamic modulation is believed to be negligible within sea ice and is therefore omitted for simulations in ice.

[27] Like other authors [*Vachon et al.*, 1993], we assume that tilt and range bunching are the dominating RAR modulation mechanisms within sea ice. It is obvious that accurate estimates for the tilt MTF are difficult to obtain as it is strongly dependent on the sea ice type. Therefore, we will start the analysis of wave damping with a method which is relatively insensitive to the RAR modulation. Only in the last section where two-dimensional wave spectra within the sea ice are retrieved T^{RAR} is required explicitly.

3.3. SAR Ocean Wave Imaging Model

[28] A SAR achieves its high azimuthal resolution by recording the Doppler history of the returned signals. As sea surface motion leads to a velocity component of a back-scattering ocean surface facet towards the radar (slant range) the corresponding SAR image points are shifted in flight direction [*Lyzenga et al.*, 1985]. This mechanism leads to an alternate stretching and bunching of image intensities in azimuth (velocity bunching). The velocity bunching effect is mainly responsible for SAR imaging of azimuth traveling waves and is in general strongly nonlinear [*Alpers and Brüning*, 1986].

[29] In the spatial domain SAR imaging of a moving sea surface with normalized radar cross section σ_0 and orbital velocity v by a SAR with platform velocity V and slant range R (distance between radar and target) is given by the following expression [*Brüning et al.*, 1990]:

$$I(\mathbf{x}) = \frac{\pi T_0^2 \rho_a}{2}\int \frac{\sigma(\mathbf{x}')}{\hat{\rho_a}(\mathbf{x}')}\exp\left(-\frac{\pi^2}{\hat{\rho}_a^2}\left(x - x' - \frac{R}{V}v(\mathbf{x}')\right)^2\right) \cdot \delta(y'-y)\,dx'dy' \tag{11}$$

Here I is the SAR intensity image, x and y are the azimuth and range coordinates, T_0 is the SAR integration time and $\hat{\rho}_a$ is the degraded azimuthal resolution

$$\hat{\rho}_a = \rho_a \sqrt{1 + \frac{T_0^2}{\tau_s^2}} \qquad (12)$$

with scene coherence time τ_s. For the ERS SAR the azimuthal resolution ρ_a is about 10 m. The orbital velocity v can be calculated to first order using the transfer function T^v (for right looking SAR).

$$T_k^v = \omega\left(\sin\theta \frac{k_y}{|k|} + i\cos\theta\right) \qquad (13)$$

Here it assumed that each fluid element exhibits a circular motion according to linear Gaussian wave theory.

[30] In this study complex SAR scenes as well as SAR intensity images are used. SAR intensity images contain information about the mean normalized radar cross section $\sigma_0 = \langle |r| \rangle^2$ observed during SAR integration time T_0, which is about 0.8 s for the ERS SAR. Complex data additionally provide information about the time evolution of σ_0 during integration time. This fact is, for example, used in the multilook technique, where two looks with half azimuthal resolution separated in time by about 0.4 s are processed. The phase shift of the cross section pattern during integration time associated with the long ocean waves can be measured based on the look cross spectrum [*Engen and Johnson*, 1995]. In particular the wave propagation direction can be determined by this technique. The technique has the additional advantage of lower noise levels in the spectral domain [*Engen and Johnson*, 1995], which is beneficial for the estimation techniques presented in this study.

[31] Equation (11) provides a mapping relation between one realization of the ocean surface and the corresponding SAR image. *Hasselmann and Hasselman* [1991] derived an integral transform for the second moments of this process, relating the ocean wave spectrum F to the SAR image variance spectrum P. This expression was later extended to include finite SAR resolution and coherence time [*Bao et al.*, 1993] as well as SAR cross spectra [*Engen and Johnson*, 1995]. The following integral transform relates F to the SAR cross spectrum P of the normalized looks $\hat{I}_i = (I_i - \langle I \rangle)/\langle I \rangle$, $i = 1, 2$ separated by the time Δt.

$$\begin{aligned} P_k(\Delta t) = & \frac{1}{4\,\pi^2} \exp\left(-k_x^2 \left(\frac{R}{V}\right)^2 f^v(\mathbf{0})\right) \exp\left(-k_x^2 \frac{\hat{\rho}_a^2}{4\pi^2}\right) \\ & \cdot \int d\mathbf{x} \exp(-i\,\mathbf{k}\,\mathbf{x}) \exp\left(k_x^2 \left(\frac{R}{V}\right)^2 f^v(\mathbf{x})\right) \\ & \cdot \left(1 + f^R(\mathbf{x}) + i\,k_x \frac{R}{V} \left(f^{Rv}(\mathbf{x}) - f^{Rv}(-\mathbf{x})\right)\right. \\ & \left. + \left(k_x \frac{R}{V}\right)^2 (f^{Rv}(\mathbf{x}) - f^{Rv}(\mathbf{0}))(f^{Rv}(-\mathbf{x}) - f^{Rv}(\mathbf{0}))\right) \end{aligned} \qquad (14)$$

Here f^R, f^{Rv}, and f^v are auto and cross correlation functions of the RAR image and the orbital velocity v.

[32] For $\Delta t = 0$ and $\hat{\rho}_a = 0$ equation (14) simplifies to the well known relation for SAR image power spectra [*Krogstad*, 1992; *Hasselmann and Hasselmann*, 1991]. For the multi look case the integration T_0 in equation (12) must be taken as the integration time of each look, e.g. $T_0 = 0.4$ s for ERS SAR. Expanding the integral part of equation (14) to first order with respect to the wave spectrum F yields the quasi-linear approximation (with $\Delta t = 0$):

$$\begin{aligned} P_k = & 0.5 \exp\left(-k_x^2 \left(\frac{R}{V}\right)^2 f^v(0)\right) \exp\left(-k_x^2 \frac{\hat{\rho}_a^2}{4\pi^2}\right) \\ & \cdot \left(|T_k^{SAR}|^2 F_k + |T_{-k}^{SAR}|^2 F_{-k}\right) \end{aligned} \qquad (15)$$

with SAR transfer function T^{SAR} given by:

$$T_k^{SAR} = T_k^{RAR} - i\,\frac{R}{V}\,k_x\,T_k^v \qquad (16)$$

The quasi-linear forward model is helpful as it allows a simple first-order retrieval of two-dimensional wave spectra from SAR image and SAR cross spectra.

3.4. Azimuthal Cutoff

[33] The main characteristics of the mapping relation given by equation (14) is a low pass filtering of the SAR image spectrum in the azimuth direction. On one hand the azimuthal cutoff leads to information loss on shorter waves traveling in the flight direction, on the other hand the width of the cutoff contains valuable information about the orbital velocity variance $f^v(0)$ caused by all ocean wave components together. As $f^v(0)$ is dominated by the high frequency part of the spectrum it is a sensitive parameter to measure the damping of short ocean waves by sea ice.

[34] The theoretical cutoff wavelength is defined [*Mastenbroek and de Valk*, 2000; *Kerbaol et al.*, 1998] as:

$$\lambda_{cut} = 2\,\pi \sqrt{\left(\frac{R}{V}\right)^2 f^v(0) + \frac{\hat{\rho}_a^2}{4\,\pi^2}} \qquad (17)$$

The dependence of λ_{cut} on coherence time and orbital velocity variance for the ERS SAR configuration is shown in Figure 4 assuming an azimuthal resolution ρ_a of 10 m (single look). As can be seen the dependence of λ_{cut} and coherence time τ_s becomes very weak if it is assumed to be longer than 50 ms. For this reason a possible increase of τ_s within the sea ice is irrelevant for the present study and therefore not considered further. Note, that the dependence of λ_{cut} on coherence time maybe stronger for airborne SAR as the R/V ratio is usually smaller in that case [*Vachon et al.*, 1993].

4. Forward Simulations

[35] In this section the impact of wave damping on the ocean wave imaging process is analyzed based on the model presented in the last section. Figure 5 shows a simulation of the two-dimensional SAR image spectrum using the full nonlinear transform equation (14) (B) and the quasi-linear linear transform equation (15) (C). A wave model spectrum with 6 m wave height and an orbital velocity variance of 1 $m^2 s^{-2}$ is used as input (A). One can clearly see the cutoff in the azimuthal (horizontal) direction discussed in the previous section. The main difference between the full nonlinear and the quasi-linear simulation is some additional

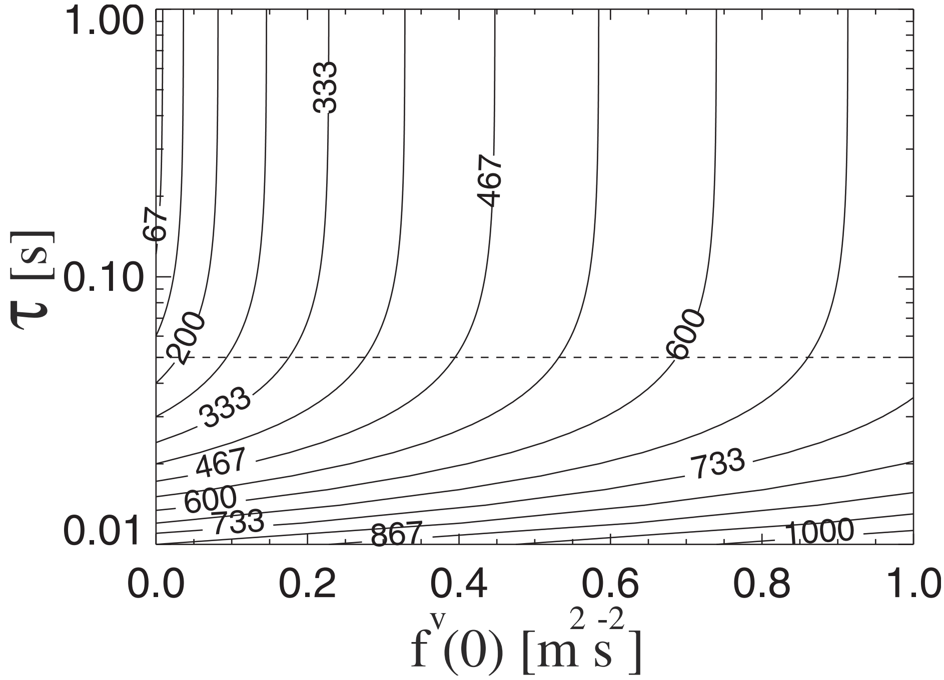

Figure 4. Theoretical cutoff wavelength λ_{cut} (compare equation (17)) depending on coherence time τ_s and orbital velocity variance $f^v(0)$.

energy observed in the cutoff region of the nonlinear simulation. For swell the difference between both simulations is negligible.

[36] As explained before, SAR imaging of range traveling waves within sea ice strongly depends on sea ice type as it is dominated by the RAR modulation mechanism. For this reason we will concentrate on the analysis of SAR imaging of azimuth waves, which is dominated by the orbital velocity of the waves. Imagine a single harmonic swell system propagating in the exact azimuth direction. The wave spectrum is thus given by

$$F(k) = \frac{H_s^2}{16}\,\delta_{k-k'} \tag{18}$$

with Dirac delta function δ, significant wave height H_s and wave number $k' = (k'_x, 0)$. The autocorrelation function of the orbital velocity v for this wave system is given by:

$$f^v(x) = \cos(k'x)\,|T^v_{k'}|^2\,\frac{H_s^2}{16} \tag{19}$$

Inserting the wave spectrum into the forward transform given by equation (14) yields:

$$P(k) = \exp\left(-k_x^2\,\omega^2\,H_s^2\left(\frac{R}{V}\right)^2\right)\sum_{n=0}^{\infty}\frac{(-1)^n\,(k_x\,\omega\,H_s\,\frac{R}{V})^{2n}}{16^n\,n!}$$
$$\cdot\int \exp(i\,k\,x)\,\cos(k'x)^n\,dx$$

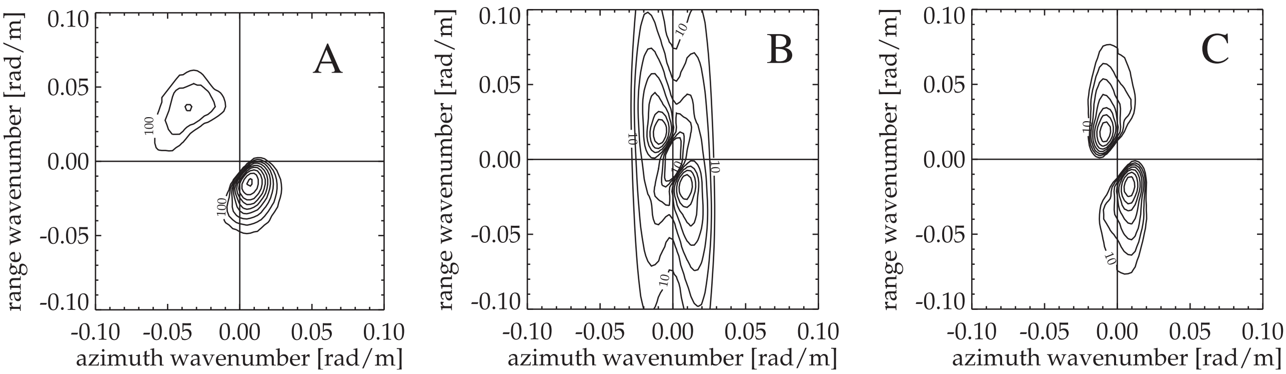

Figure 5. (a) Two-dimensional WAM ocean wave model spectrum with 6 m wave height and 1 $m^2\ s^{-1}$ orbital velocity variance showing a 100 m wind sea and a 300 m swell system. Simulated SAR image spectra based on (b) the full nonlinear model (equation (14)) and (c) the quasi-linear model (equation (15)). Isolines are logarithmically spaced with five isolines per decade and labels given in m^4 for the wave spectrum and m^2 for the image spectra.

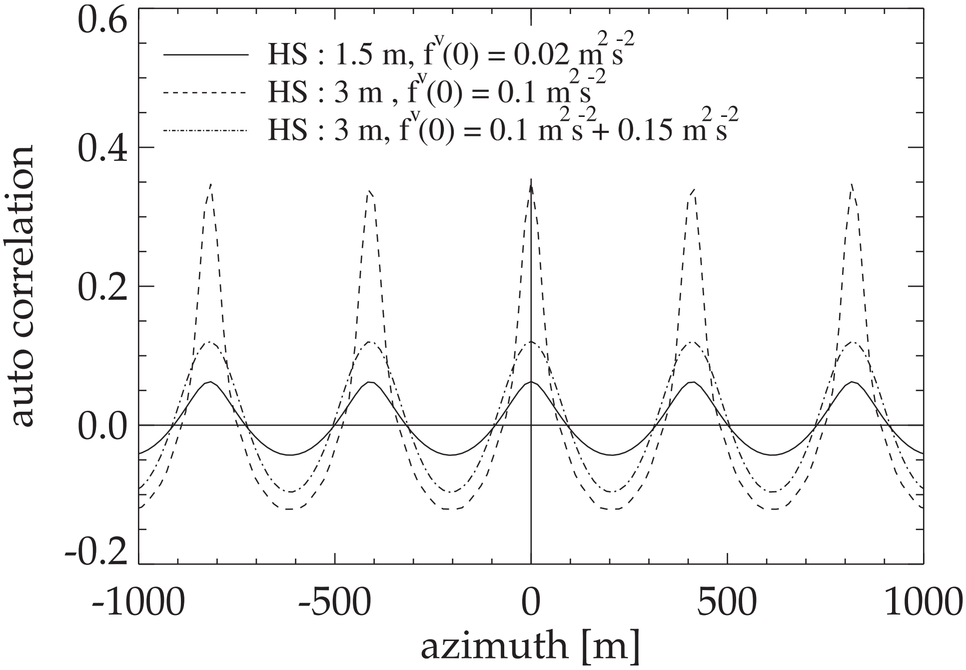

Figure 6. Simulated azimuthal SAR image autocorrelation function assuming a harmonic swell system of 400 m wavelength with 1.5 (solid line) and 3 m wave height (dashed line) propagating in the exact azimuth direction. The dashed dotted line results if an additional wind sea system (7 ms^{-1} wind speed) is assumed.

$$= \exp\left(-k_x^2\,\omega^2\,H_s^2\left(\frac{R}{V}\right)^2\right)\sum_{n=0}^{\infty}\frac{(-1)^n\,(k_x\,\omega\,H_s\,\frac{R}{V})^{2n}}{32^n\,n!} \cdot \bigotimes_{j=1}^{n}(\delta_{k'-k}+\delta_{k'+k}) \quad (20)$$

Here the small RAR modulation for an azimuth wave was neglected and the exponential factor under the integral was expanded. Furthermore, it was used that $|T_k^v| \approx \omega_k$ for small incidence angles (compare equation (13)). The convolution operator is denoted by $\otimes$. The image spectrum has energy at wave numbers $k = j\,k_x'$, $j = \pm1, \pm2, \pm3,\ldots$ and extends out to $k = \pm\,nk_x'$ for nonlinearity order n. Furthermore it can be seen that the higher harmonics increase with growing wave height, frequency, and R/V ratio until the cutoff factor in front of the integral starts to dominate.

[37] A simulation based on equation (20) is shown in Figure 6. A swell system of 400 m wavelength is assumed to propagate in the azimuth direction. The solid and the dashed line represent the resulting azimuthal SAR image autocorrelation functions (calculated by taking the Fourier transform of equation (20)) for 1.5 m and 3 m wave height respectively. The orbital velocity variance caused by the swell is 0.02 and 0.1 m^2 s^{-2}, respectively. The dashed dotted line indicates the correlation function if an additional wind sea system, which increases the orbital velocity variance by 0.15 m^2 s^{-2} is assumed. The latter case shows the typical situation in the open ocean where the higher harmonics of the swell system image are suppressed by an additional wind sea system. The solid and dashed lines illustrate the situation within the sea ice, where wind seas are damped leading to a spiky appearance of the image of strong swell systems in sea ice.

4.1. Impact of Sea Ice on Orbital Velocity Variance

[38] As explained in the last section imaging of waves traveling in azimuth direction is strongly influenced by the orbital velocity variance of the sea surface. The contribution to the orbital velocity of wind sea and swell systems can be estimated using simplified models. To study the sea ice impact an ice cutoff wave number is introduced.

[39] For small incidence angles θ the orbital velocity variance $f^v(0)$ can be approximated as (compare equation (13))

$$f^v(0) \approx \int \omega^2\,F_{\mathbf{k}}\,d\mathbf{k} \quad (21)$$

Based on this relation a first-order analysis of the impact of short wave damping on $f^v(0)$ can be carried out. A simple model for a wind sea spectrum with peak wave number k_p, which is chopped off by sea ice at some wave number k_{ice} is given by

$$\int F_{\mathbf{k}}\,d\Phi = \begin{cases} 0 & : \quad k \le k_p \ \text{ or } \ k \ge k_{ice} \\ \alpha\,k^{-4} & : \quad \text{else} \end{cases} \quad (22)$$

The k^{-4} decay assumed in this model corresponds to a ω^{-5} decay in the corresponding one-dimensional frequency spectrum [*Hasselmann*, 1973]. Inserting the model equation (22) in equation (21) gives

$$f^v(0) = \begin{cases} \alpha\,g\,(\frac{1}{k_p} - \frac{1}{k_{ice}}) & : \quad k_p \le k_{ice} \\ 0 & : \quad \text{else} \end{cases} \quad (23)$$

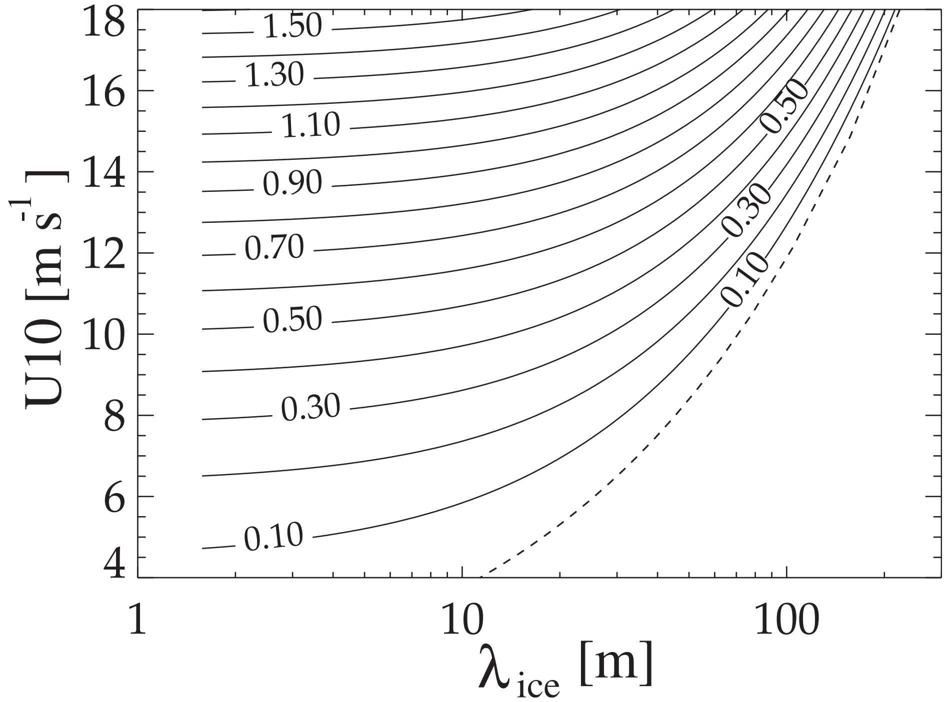

Figure 7. Orbital velocity variance $f^v(0)$ for a fully developed wind sea as a function of wind speed U_{10} and ice cutoff wavelength λ_{ice}. The dashed line indicates the peak wavelength for a given wind speed. The unit for $f^v(0)$ is $m^2\ s^{-2}$.

It is further assumed that in the open water the wind sea is fully developed with phase speed $c_p = \sqrt{g/k}$ (deep water) and wave age $U_{10}/c_p = 0.95$. Using the known relationship $H_s = 0.24\ U_{10}^2/g$ between wind speed U_{10} and significant wave height H_s the constant $\alpha = 4.5 \cdot 10^{-3}$ is obtained. The dependence of $f^v(0)$ on U_{10} and the ice cutoff wavelength $\lambda_{ice} = 2\ \pi/k_{ice}$ is illustrated in Figure 7. The dashed line indicates the peak wavelength for a fully developed wind sea in the open ocean. The orbital velocity variance of a 100 m system is about 0.6 $m^2\ s^{-2}$ in the open water. It decreases to 0.3 $m^2\ s^{-2}$ if waves shorter than 40 m are damped out by the ice.

[40] As swell is concentrated in a relatively small region of the 2d wave spectrum equation (21) can be approximated as

$$f^v(0) \approx \frac{\pi g}{8\,\lambda_{swell}}\ (H_s^{swell})^2 \qquad (24)$$

with swell wavelength λ_{swell} and swell wave height H_s^{swell}. The wavelength and wave height dependence of $f^v(0)$ for swell is illustrated in Figure 8. A 400 m meter swell system with 3 m wave height contributes about 0.1 $m^2\ s^{-2}$ to the orbital velocity variance of the sea surface. Thus, in the open ocean the swell contribution to $f^v(0)$ is in general smaller than the contribution coming from the wind sea. The azimuthal cutoff is therefore highly dependent on the local wind field.

5. Azimuthal Cutoff Estimation

[41] Neglecting the small influence of coherence time τ_s, the orbital velocity variance is directly connected to the theoretical cutoff wavelength λ_{cut}. This means the SAR measurement of $f^v(0)$ is basically a cutoff estimation problem.

[42] Different definitions and estimation techniques have been proposed for empirical cutoff wavelengths [*Kerbaol et al.*, 1998; *Vachon et al.*, 1997; *Hasselmann et al.*, 1996]. In this study we follow the approach developed by *Kerbaol et al.* [1998], where a cutoff wavelength λ_{Kerb} is estimated in the spatial domain. The model function

$$C(x) = \exp\left(-\pi^2\,\frac{x^2}{\lambda_{Kerb}^2}\right) \qquad (25)$$

is fitted to the azimuthal cross-correlation function of two looks processed from the azimuth spectrum of complex SAR data [*Kerbaol et al.*, 1998]. In order to use λ_{Kerb} to estimate the theoretical λ_{cut} a global data set of about 1000 WAM ocean wave model spectra from the ECMWF was used to calculate a linear regression between both parameters. For each wave spectrum the model equation (25) was fitted to the simulated cross-correlation function calculated by taking the Fourier transform of equation (14). As the highest frequency in the WAM model is f_{max} = 0.4 Hz corresponding to about 10 m wavelength the net contribution to $f^v(0)$ from waves shorter than 10 m was calculated by extrapolating the one-dimensional frequency spectrum with a f^{-5} tail, e.g. the following term is added to $f^v(0)$.

$$\langle v^2\rangle_{Hf} = 2\,\pi^2\,F(f_{max})\,f_{max}^3 \qquad (26)$$

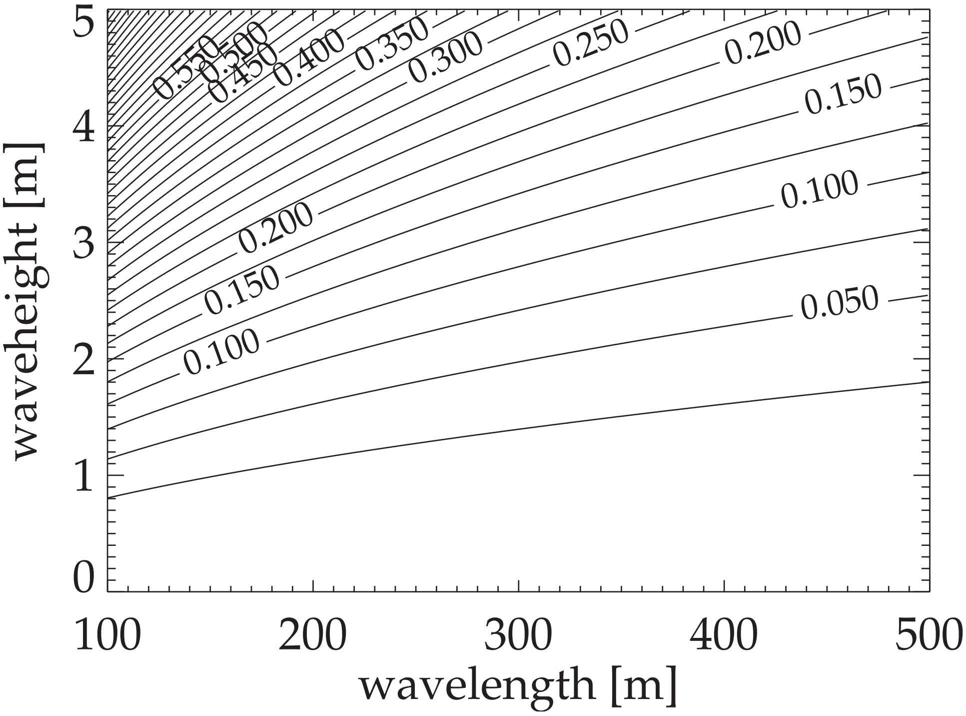

Figure 8. Orbital velocity variance in $m^2 s^{-2}$ caused by swell as a function of wavelength and significant wave height.

The corresponding scatter plot is shown in Figure 9 (left). The linear regression with a correlation of 0.98 is given by:

$$\lambda_{cut} = 2.2 \cdot \lambda_{Kerb} + 37.0\ m \tag{27}$$

The resulting empirical relation between λ_{Kerb} and the orbital velocity variance $f^v(0)$ is shown in Figure 9 (right).

6. Case Studies

6.1. Case Study I, Weddell Sea

[43] Figure 10 (left) shows a 5 × 10 km ERS-2 SAR scene acquired over the Weddell Sea on July 18, 1992, 12:41 UTC (Orbit 5264, Frame 4815). The image is centered at 58.98°S, 52.9°W with flight direction (205°) upwards. Following the bright open water area two different

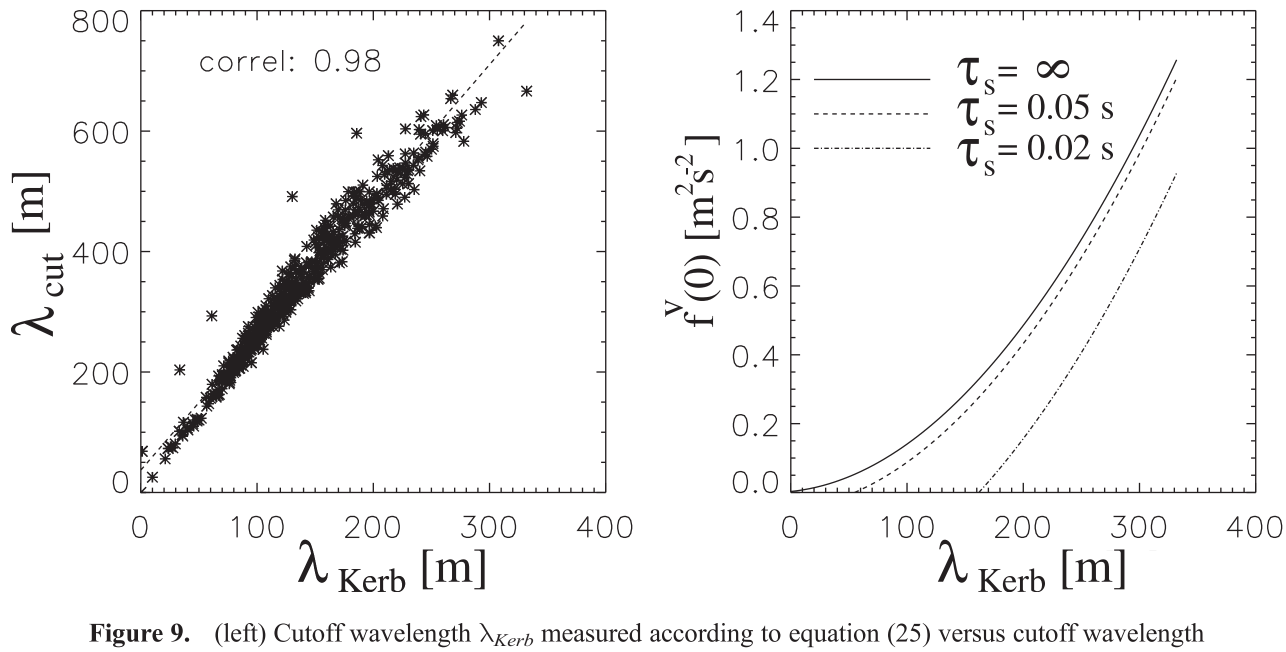

Figure 9. (left) Cutoff wavelength λ_{Kerb} measured according to equation (25) versus cutoff wavelength defined by equation (17). The plot is based on simulations using 1000 ECMWF wave model spectra. (right) Resulting relationship between λ_{kerb} and the orbital velocity variance assuming coherence times τ_s of 0.02 s, 0.05 s and infinity.

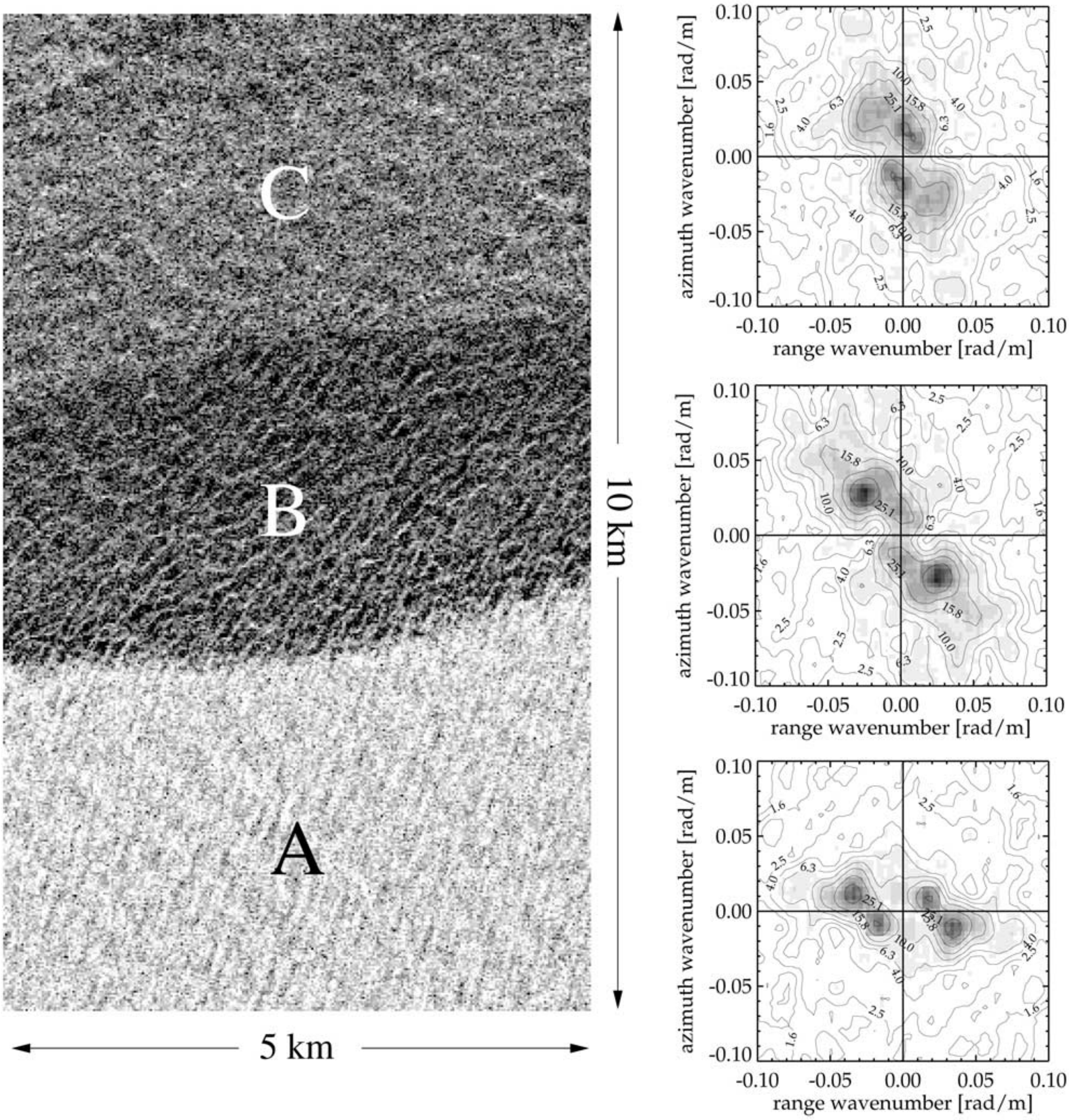

Figure 10. (left) 5 × 10 km ERS-2 SAR scene acquired over the Weddell Sea on July 18, 1992. The bright region at the bottom is open water followed by two darker regions, that are covered by two different types of sea ice. (right) Image spectra calculated for regions A, B, and C.

types of sea ice with significantly different NRCS values can be seen. The typical situation at the ice boundary is that the open water is followed by grease or brash ice, which completely damps out the short Bragg waves, leading to the low radar backscatter observed on the SAR image. The grease ice area is then usually followed by a region with small ice floes (pancake ice) with slightly higher radar cross section than grease ice.

[44] The SAR wind measurement technique described by *Lehner et al.* [1998] and *Horstmann et al.* [2000] was applied yielding about 11 m s^{-1} wind speed. The method is based on the CMOD4 model originally developed for the scatterometer and requires calibration of the SAR images. The wind direction of about 340° (coming from) can be derived from wind streaks observed in the open water. The wind direction is confirmed by the observation of a very sharp ice boundary, which is typical if strong wind is blowing from the open ocean towards the sea ice.

[45] The SAR image spectra on the right hand side of Figure 10 show two-wave systems of about 180 and 300 m

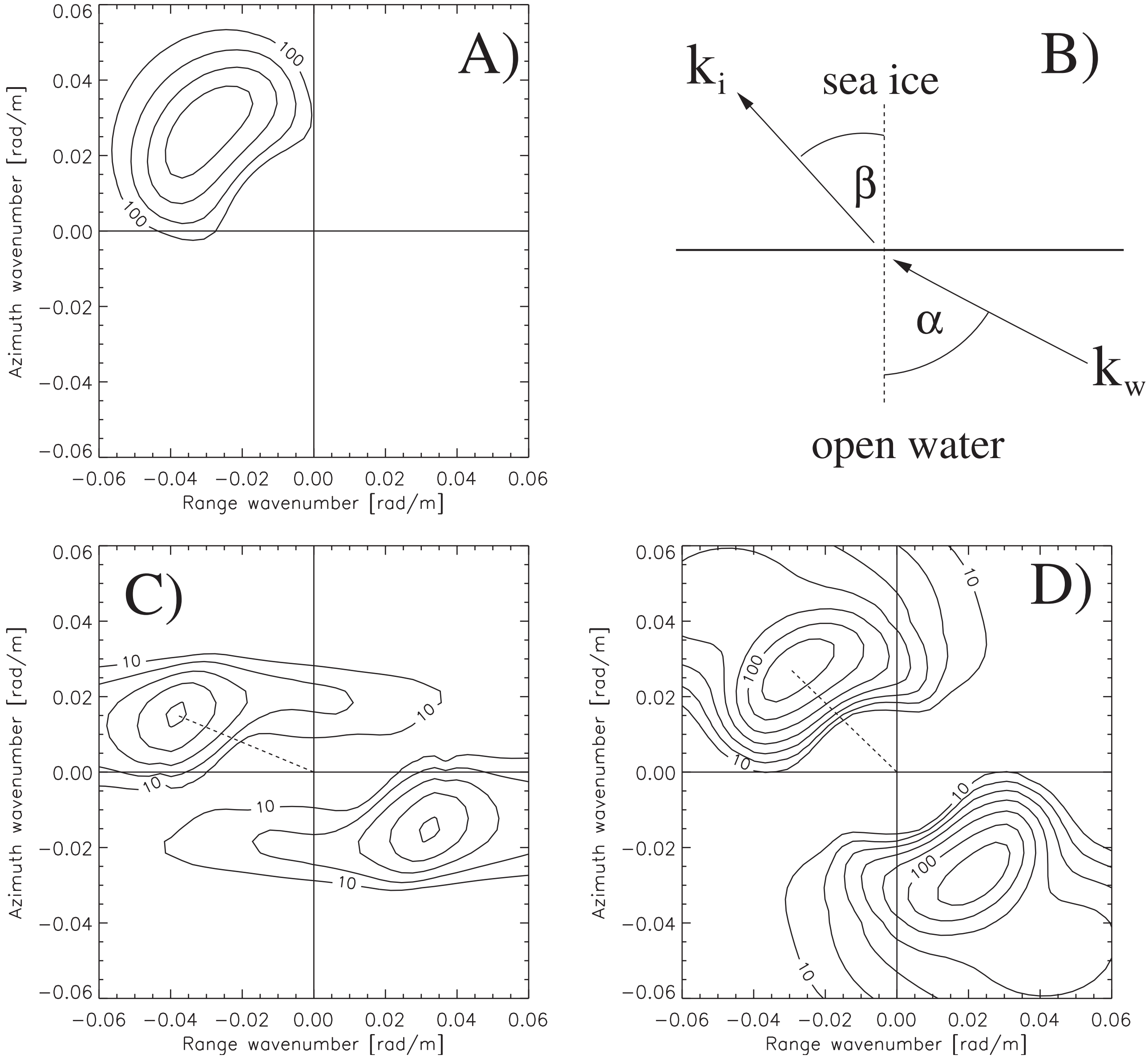

Figure 11. Simulation showing that refraction phenomena at the ice boundary observed on SAR images can be imaging artifacts caused by damping of short ocean waves. (a) Parameterized ocean wave spectrum (JONSWAP) representing a 150 m ocean wave system, (b) schematic illustration of refraction mechanism (compare equation (3)), (c) simulated SAR image spectrum in open water, and (d) SAR image spectrum in sea ice, simulated by removing ocean wave components shorter than 80 m.

wavelength propagating into the ice. A quasi-linear inversion of the spectrum in the open water gave about 2 m wave height for the 180 m wave and 1 m wave height for the 300 m wave system. In the grease and brash ice region one can see the 180 m wave being refracted towards the normal of the ice boundary by about 15°. The image modulation is increased by about 3 dB at the same time. In the upper ice area the 180 m wave is almost invisible in the image.

[46] In some studies refraction phenomena like the observed one are interpreted as a real refraction of the ocean waves at the ice boundary [*Shuchman and Rufenach*, 1994]. However, applying the mass load model described in section 2 to the observed refraction yields an unrealistic ice coverage with $c\ h \approx 5$ m. This means that the observed refraction is in fact mainly a SAR imaging artefact, which is due to damping of short waves by the ice. Figure 11 shows a simulation, which illustrates this refraction effect. SAR image spectra were simulated in open water (C) as well as in sea ice (D) using a parameterized JONSWAP [*Hasselmann et al.*, 1980] ocean wave spectrum (A) representing a 150 m wave system. The simulations are based on the forward model equation (14), where the sea ice impact was simulated by removing all waves shorter than 80 m. Comparing the SAR spectra in water and ice one can see that short wave damping is in fact able to cause refraction phenomena like the observed one. The inversion scheme presented in section 5 will use the change of the two-dimensional SAR spectra to gain quantitative information on the ice damping characteristics.

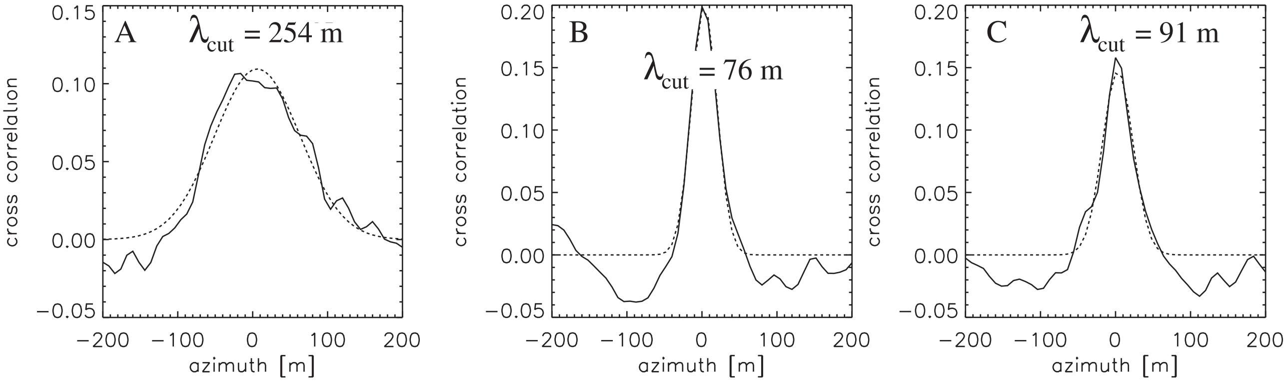

Figure 12. Azimuthal correlation functions calculated in regions A, B, and C as indicated in Figure 10. The dashed lines are the respective fits of the Gaussian model defined in equation (25).

[47] To study the wave damping a cutoff analysis as described in section 5 was performed. The azimuthal autocorrelation functions calculated for regions (A), (B), and (C) are shown in Figure 12. In the open water a cutoff wavelength of λ_{Kerb} = 254 m was found. From the relationship between λ_{Kerb} and $f^v(0)$ derived in section 5 (compare Figure 9 (right)) the orbital velocity in the open water is estimated as 0.7 m^2 s^{-2}. This is consistent with the general theoretical findings about the orbital velocity variance of wind seas and swell systems presented in section 4; the contribution of the two long wave systems to the orbital velocity variance is about 0.1 m^2 s^{-2} with the main contribution coming from the 180 m wave system (compare Figure 8). Assuming a fully developed wind sea the measured wind speed leads to a wind sea system of about 2 m wave height and 80 m wavelength which contributes another 0.6 m^2 s^{-2} to the orbital velocity variance (compare Figure 9). This results in a total velocity variance of about 0.7 m^2 s^{-2} confirming the value obtained by the cutoff estimation technique. Note that the wind sea is not visible on the SAR image as it is propagating in the approximate azimuth direction and therefore suppressed by the azimuthal cutoff.

[48] In region (B) of Figure 10 the cutoff wavelength decreases to 76 m, which corresponds to an orbital velocity variance of about 0.05 m^2 s^{-2}. This decrease can only be explained if it is assumed that the wind sea is almost completely damped out by the ice. As explained in section 2 this is realistic, as e-folding distances of down to 1–2 km have been observed in earlier field campaigns reported by *Wadhams et al.* [1988] (compare Figure 1). As a complete damping of the wind sea still leaves about 0.1 m^2 s^{-2} velocity variance it can be concluded that also the wave height of the 180 m wave must have been reduced by about 3 dB to obtain the observed value for $f^v(0)$ within region (B) (compare Figure 8).

[49] In region (C) the observed cutoff wavelength is 91 m, which corresponds to about 0.05 m^2 s^{-2} as in region (B). This observation confirms that the damping of the 180 m wave is moderate as one would expect a stronger decrease of $f^v(0)$ otherwise.

6.2. Case Study II, Greenland Sea

[50] Figure 13 (A) shows a 100 × 130 km ERS-2 SAR scene (Orbit 2856, Frame 1341 and part of Frame 1359) acquired over the Greenland Sea on Feb 1, 1992, 23:32 UTC. The image is centered at 66° 45′0″N, 28° 47′49″W with flight direction (342°) upwards and shows the marginal ice zone with dark areas corresponding to sea ice and bright areas indicating open water.

[51] The SAR wind measurement technique described by *Lehner et al.* [1998] was applied, giving about 12 m s^{-1} wind speed. The wind direction of about 70° (coming from) can be derived from wind streaks observed in the open water area and is indicated by an arrow in Figure 13. The directional ambiguity of wind direction was resolved comparing to ECMWF wind fields. The indicated wind direction is also suggested by the observation of a very sharp ice edge on the east side of the ice covered area and a more fuzzy appearance of the westerly ice boundary.

[52] Three 5 × 5 km subimages taken from locations (A), (B), and C indicated in Figure 13 are shown in Figure 14 together with the modulus of the corresponding cross spectra. At location (C) a wind sea system of about 80 m and a swell system of about 350 m wavelength can be seen traveling in easterly and north westerly direction respectively. The directional propagation ambiguity was resolved by inspection of the imaginary part of the cross spectrum. The wind sea system is not visible in the sea ice (location B) nor in the open water at location (A). For the swell a significant reduction of image modulation of about −4 dB is observed comparing locations (A) and (C). This effect becomes more obvious looking at the one-dimensional wave number spectra shown in Figure 15.

[53] A wind speed of 12 m s^{-1} results in a fully developed wind sea of about 100 m wavelength and 3 m wave height. The observed wavelength of 80 m is in reasonable agreement with the theoretical value indicating that the wind sea is almost fully developed. As the wind sea is not visible in area (A) it can be assumed that it is damped out completely by the ice. This finding is again consistent with in situ measurements which yield e-folding distances down to 1–2 km for 100 m waves (compare Figure 1).

[54] Applying the cutoff estimation technique described in section 5 gives λ_{Kerb} = 210 m for area A, λ_{Kerb} = 92 m for the ice covered region and λ_{Kerb} = 296 m for region C (compare Figure 16). For area (C) where both wave systems are visible this yields an orbital velocity variance of 0.9 m^2 s^{-2} (compare Figure 9(right)). Assuming that the wind sea contributes between 0.7 and 0.8 m^2 s^{-2} to $f^v(0)$ (compare Figure 7) it can be concluded that the swell

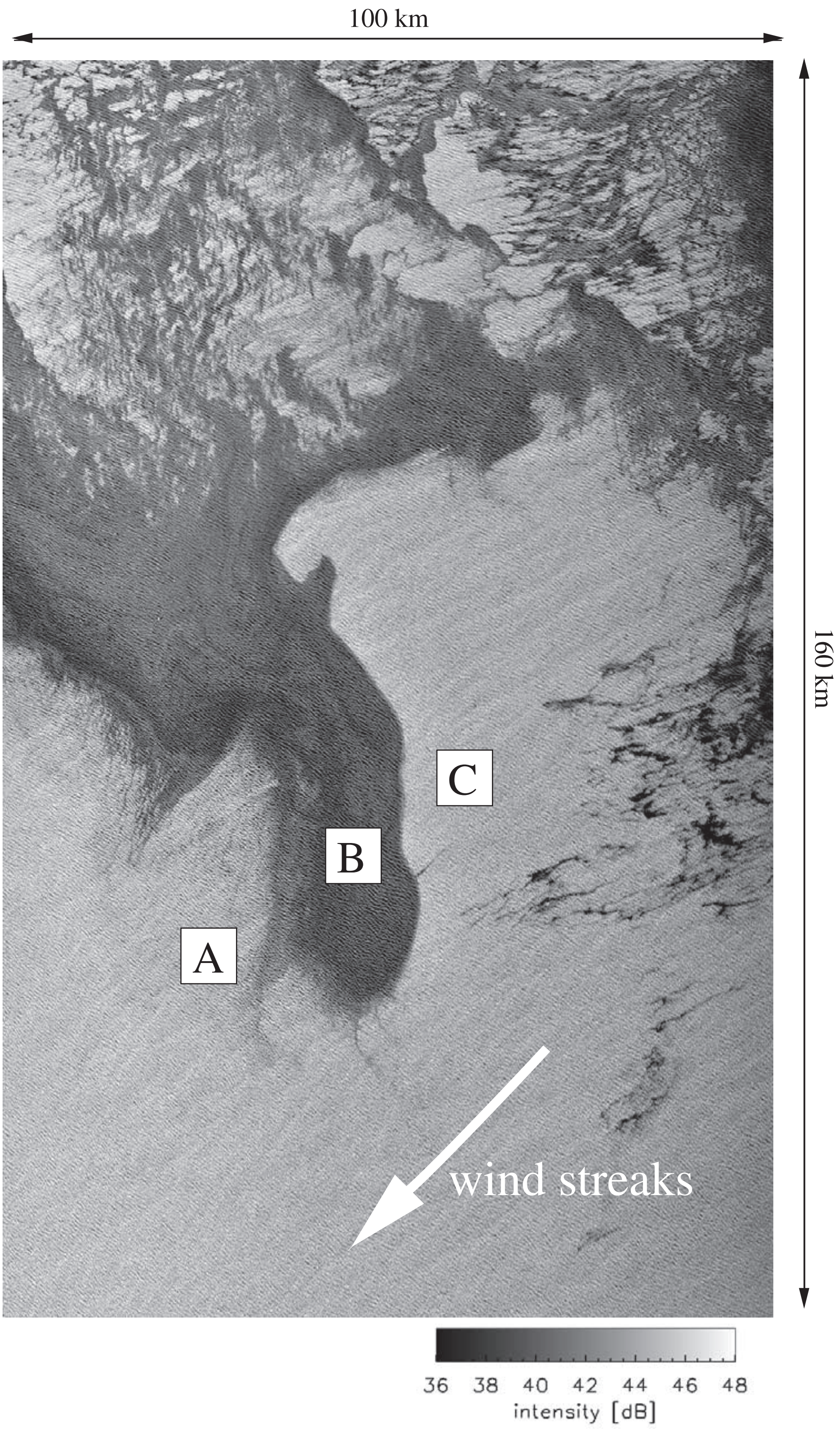

Figure 13. The 100 × 130 km ERS-2 SAR scene acquired over the Greenland Sea centered at 66° 45′0″N, 28° 47′49″W on February 1, 1992, 2332 UTC, showing the marginal ice zone. The bright region is open water, while the darker areas are covered with sea ice.

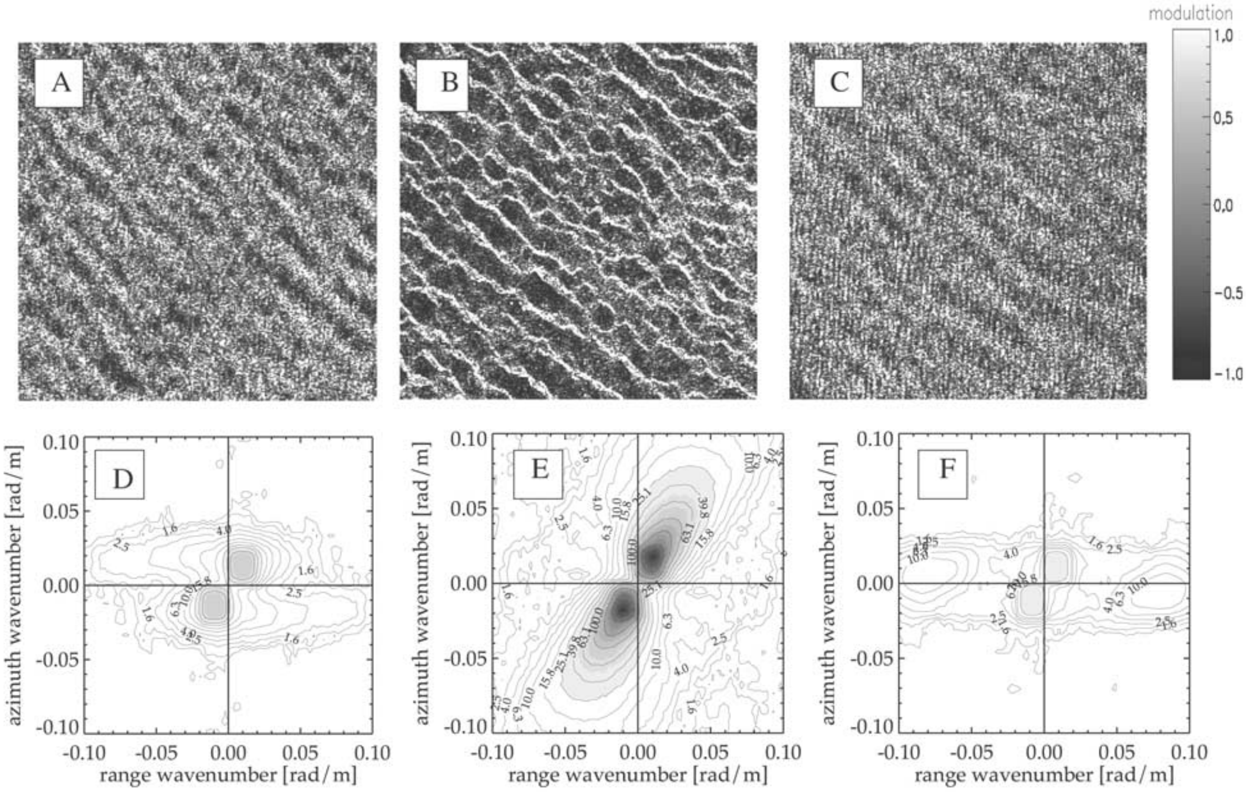

Figure 14. (top) The 5 km by 5 km subimages extracted from locations A, B, and C indicated in Figure 13. Gray values correspond to SAR image modulation. (bottom) Modulus of corresponding SAR cross spectra with identical scaling of gray values. The isolines are logarithmically spaced with five isolines per decade, and labels are given in m^2.

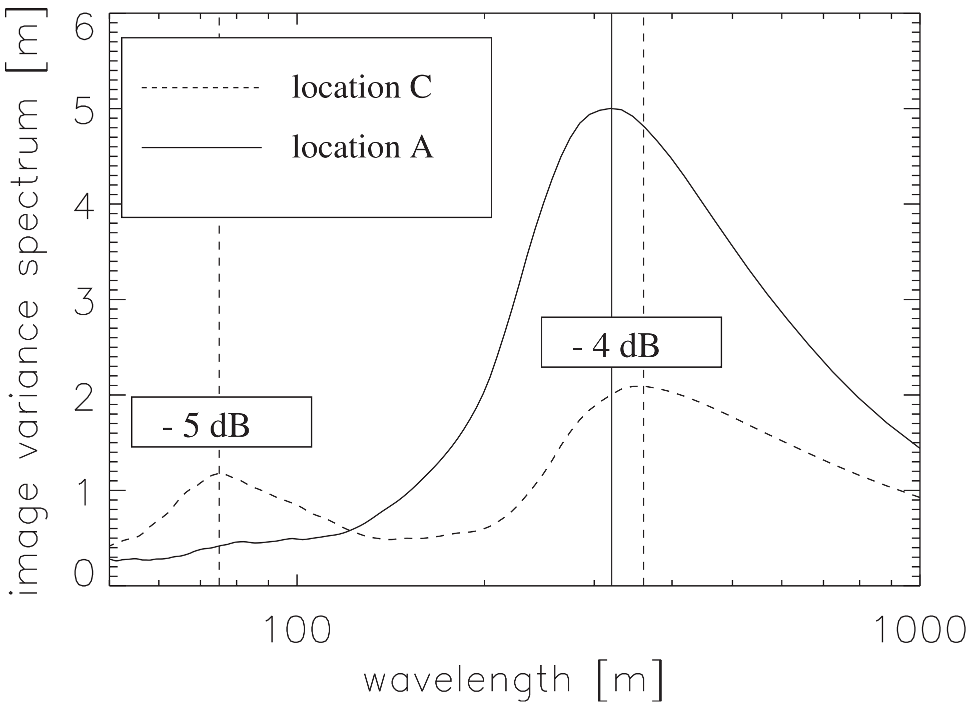

Figure 15. One-dimensional SAR image variance wave number spectra for locations A (solid) and C (dashed) indicated in Figure 13.

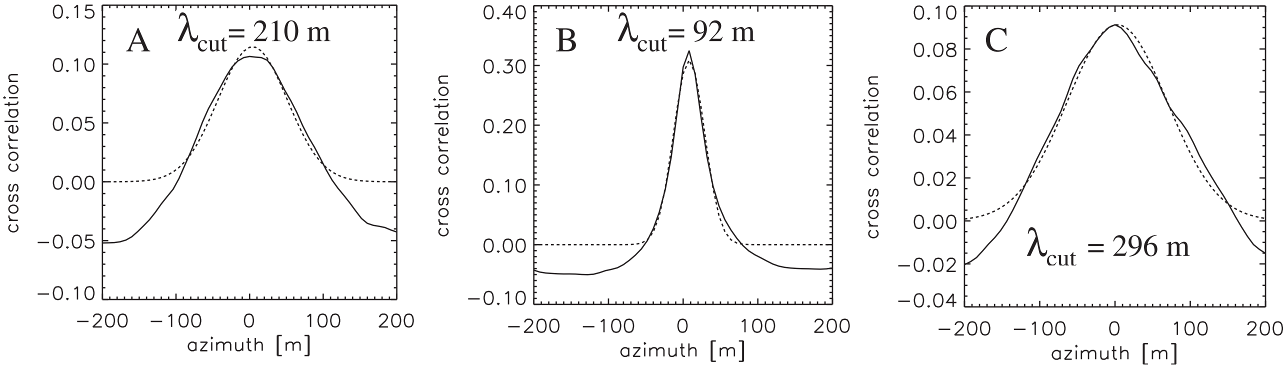

Figure 16. Azimuthal look cross-correlation functions with fitted Gaussians calculated from subimages shown in Figure 14. Cutoff wavelengths were estimated using the model equation (25).

contributes between 0.1 m^2 s^{-2} and 0.2 m^2 s^{-2} and thus has a wave height between 3 and 4 m (compare Figure 8).

[55] In the ice $f^v(0)$ decrease to about 0.1 m^2 s^{-2} which is consistent with the assumption that the wind sea is damped out completely and that the long swell is only slightly affected.

[56] In region (A) where only the swell system is visible on the SAR image the estimated orbital velocity variance is about 0.5 m^2 s^{-2}. This is due to the generation of new short waves by the wind, which contribute about 0.4 m^2 s^{-2} to $f^v(0)$. Note, that the new waves are too short to be visible on the SAR image; the range resolution of the ERS SAR is about 30 m, e.g., waves must have wavelength well over 60 m to be imaged by the system. However, at 11 m s^{-1} wind speed a fetch between 50 and 100 km is required to generate waves of such length [*Apel*, 1995]. As there is only about 30 km open water visible on the SAR image left of the ice region the new waves cannot be detected.

7. A New SAR Ocean Wave Inversion Scheme for the MIZ

[57] In this section a new SAR inversion scheme for ocean waves in ice is presented. The method is based on studies of short ocean wave attenuation described in the previous chapters. The algorithm uses models and techniques which have already been successfully used for ocean waves in open water.

[58] The method derives damping parameters of the sea ice by combined use of SAR information from the ice region, the open water in front of the ice, and information from an ocean wave model. The output of the algorithm is a two-dimensional ocean wave spectrum in front and behind the ice boundary as well as a two-dimensional filter function characterizing the sea ice impact on the wave spectrum.

[59] Similar to the approach presented by *Hasselmann and Hasselmann* [1991], the inversion scheme is based on minimisation of the following cost function:

$$J(F,\tilde{\rho}) = \int G_k\,(\tilde{P}^W_k - P^W_k(F))^2 + \overline{G}_k\,(\tilde{P}^I_k - P^I_k(B^{\tilde{\rho}}\,F))^2 + H_k\,(\hat{F}_k - F_k)^2 + V_k\,(\hat{F}_k\,F_{-k} - \hat{F}_{-k}\,F_k)^2\;\;dk \quad (28)$$

Here G_k, $\overline{G_k}$, H_k and V_k are weighting functions and $B^{\tilde{\rho}}$ is a parameterized filter function describing the sea ice impact on the ocean wave spectrum. An ocean wave spectrum F and damping parameters $\tilde{\rho} = (\rho_1,\ldots,\rho_l)$ are determined such that the deviation between the simulated SAR spectra $P^W_K(F)$ and $P^I_k\left(B^{\tilde{\rho}}F\right)$ in open water and sea ice and the corresponding observations $\tilde{P}^W_k$ and $\tilde{P}^I_k$ is small. In a first approach P^W_k and P^I_k were calculated by using the quasi-linear approximation (equation (15)). The only difference between P^I_k and $\tilde{P}^W_k$ is a neglecting of the hydrodynamic modulation for waves in ice (compare section 3).

[60] In addition, equation (28) contains two regularization terms. By appropriate choice of the weighting functions, the first term ensures that missing information on short azimuthal waves is taken from the first guess ocean wave spectrum $\hat{F}$. The second term forces the algorithm to take the propagation direction of the long ocean waves, or more precisely the ratio of F_k and F_{-k} from the first guess.

[61] Due to different observations suggesting that sea ice acts like a filter with steep flanks on the ocean wave spectrum (compare section II), the filter function $B^{\tilde{\rho}}_k$ was in a first approach taken as a Butterworth filter.

$$B^{(\gamma,\tilde{k})}_k = \left(1 + \left(\frac{|k|}{\tilde{k}}\right)^{\gamma}\right)^{-1} \quad (29)$$

The filter is isotropic with 3dB width given by $\tilde{k}$. The flank steepness can be controlled by appropriate choice of γ.

[62] To solve the minimization problem given by equation (28) a new technique was developed using the quasi-linear approximation (equation (15)). The approach is based on the following Lagrange function [*Spellucci*, 1993]:

$$L(F,\tilde{\rho},\alpha,\overline{\alpha},\lambda_\alpha,\lambda_{\overline{\alpha}}) = J(F,\tilde{\rho}) - \quad (30)$$

$$\lambda_\alpha\left(\alpha - \int |T^v_k|^2 F_k\;dk\right) - \quad (31)$$

$$\lambda_{\overline{\alpha}}\left(\overline{\alpha} - \int |T^v_k|^2 B^{\tilde{\rho}}_k F_k\;dk\right) \quad (32)$$

The new state variables α, $\overline{\alpha}$ represent the orbital velocity variance in open water and in the sea ice region, respectively. Introducing the Lagrange parameters λ_α and $\lambda_{\overline{\alpha}}$, the derivative of equation (28) with respect to F becomes linear. Using the necessary conditions for a solution of the

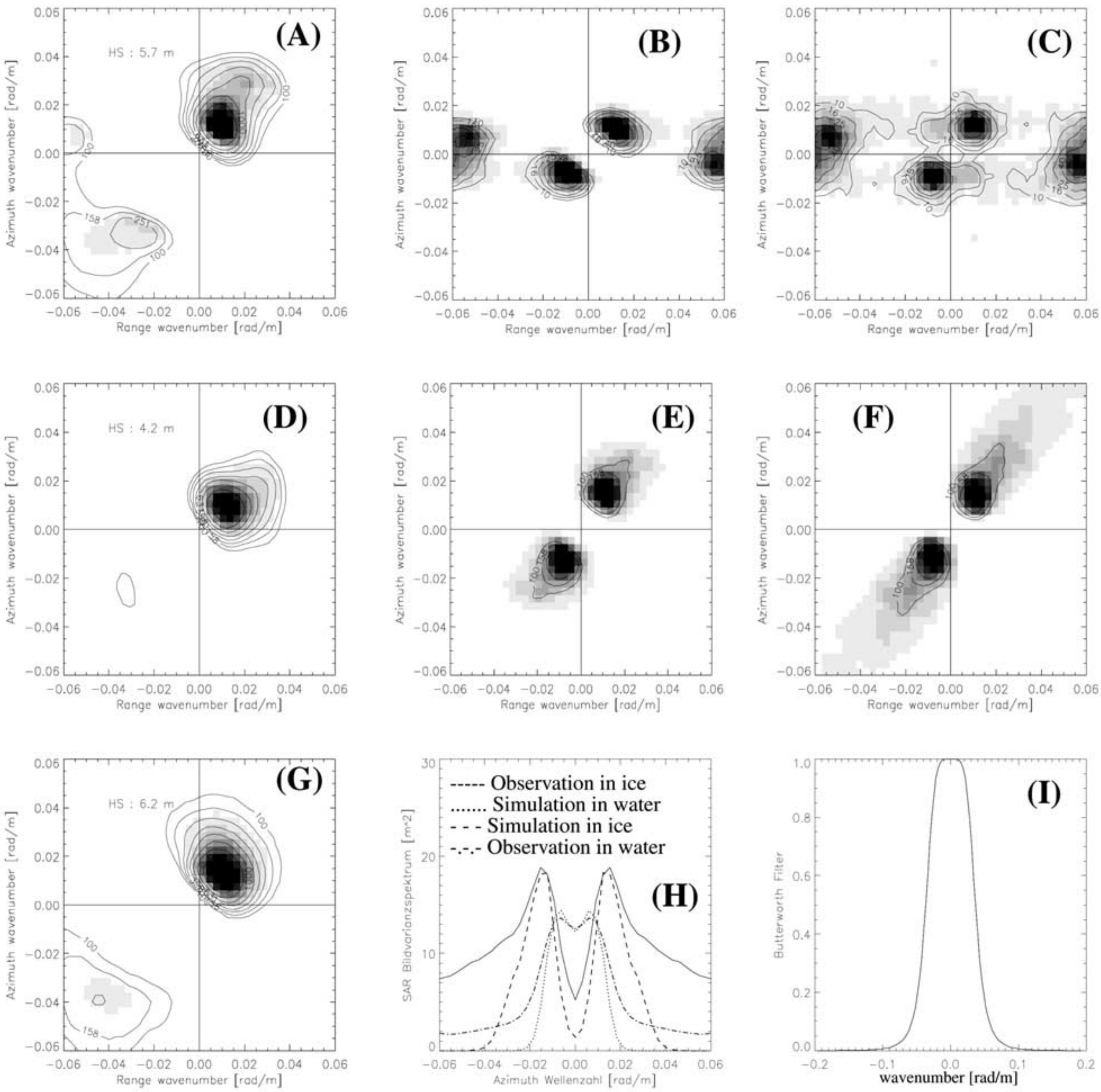

Figure 17. (a) Inverted ocean wave spectrum in open water. (b) Simulated SAR image spectrum in open water. (c) SAR image spectrum observed in open water. (d) Inverted ocean wave spectrum in sea ice. (e) Simulated SAR image spectrum in sea ice region. (f) SAR image spectrum observed in sea ice. (g) First guess ocean wave spectrum computed with the WAM model. (h) Comparison of simulated and observed cutoff in open water and sea ice. (i) Calculated Butterworth filter with $\gamma = 10$ and $\tilde{k} = 0.036$ rad/m.

optimization problem, F can therefore be expressed as a function of α, $\overline{\alpha}$, $\tilde{\rho}$, λ_{α}, $\lambda_{\overline{\alpha}}$. Denoting the number of filter parameters with l, the remaining equations lead to a $4 + l$-dimensional zero crossing problem, which can be solved very efficiently using a Newton method.

[63] The method was applied to the ERS SAR scene discussed in section 6.2. Figure 17 shows results of the inversion. The SAR spectra observed in the ice and the open water are shown in (C) and (F), respectively. The first guess ocean wave spectrum calculated with the WAM model can be seen in (G). In this first example only the filter width $\tilde{k}$ was optimized, while the second parameter was fixed to $\gamma = 10$, assuming a nearly rectangular filter shape. The algorithm was run using different start approximations for the Newton method.

[64] The algorithm converged in 90% of the cases, yielding exactly identical solutions. The inverted ocean wave spectra in sea ice and open water are shown in (A) and (D). The wave spectrum behind the ice boundary is calculated by applying the Butterworth filter shown in (I) to the open water wave spectrum. The algorithm calculated a filter width of $\tilde{k} = 0.036$ rad/m, leading to a reduction of the orbital

velocity variance from $\alpha = 1$ m^2 s^{-2} in the open water, down to $\overline{\alpha} = 0.13$ m^2 s^{-2} in sea ice. Note that the estimated orbital velocity variance is in good agreement with the estimates of $f^v(0) = 0.9$ m^2 s^{-2} and $f^v(0) = 0.1$ m^2 s^{-2} found by the simple cutoff estimation technique (compare section 6.2). As can be seen, there is good agreement between the simulated and the observed SAR image spectra in open water as well as in ice. Although the cutoff comparison shown in (H) indicates an underestimation of energy contained in short azimuth waves, the azimuthal widening of the spectrum as well as the long wave energy increase are reproduced by the simulation.

[65] The presented algorithm can be extended for use with SAR cross spectra [*Engen and Johnson*, 1995] using standard methods. In this case the second regularization term can be omitted, as the propagation direction of the long waves is contained in the complex SAR data. In addition the approach described in [*Hasselmann and Hasselmann*, 1991] can be used to introduce the full nonlinear forward model into the algorithm. It is expected that this extension will lead to an even better reproduction of the observed cutoff change.

8. Conclusions and Outlook

[66] Damping of ocean waves traveling into sea ice was studied using spaceborne SAR data acquired over the MIZ. Typical imaging artifacts like spiky wave crests and wave refraction were analyzed theoretically. It was shown that the observed effects can be explained by damping of the high frequency part of the ocean wave spectrum. A possible increase of the coherence time of the complex reflectivity within sea ice, was shown to have a minor impact for ERS SAR data.

[67] A simple and robust method originally developed for wind speed measurements was applied to estimate the orbital velocity variance of the sea surface in the open water as well as in the sea ice. The method has the advantage to be relatively insensitive to the RAR modulation, which is in general not accurately known for sea ice. An azimuthal cutoff wavelength calculated from the SAR image autocorrelation function was related to the orbital velocity variance by regression. A linear relationship was fitted based on nonlinear forward simulations of the azimuthal image autocorrelation function using a global data set of ocean wave model data.

[68] The orbital velocity variance was then used as a parameter to estimate ocean wave damping. Sensitivity studies were carried using models for wind sea and swell systems. Simple analytical expressions were derived for the contribution of swell and wind sea to the orbital velocity variance depending on wind speed, swell wave height and wavelength.

[69] The method was applied to ERS SAR scenes acquired over the Weddell and the Greenland Sea. It was shown that the estimated attenuation rates are consistent with measurements obtained in earlier field campaigns in the Greenland and Bering Sea.

[70] In a second step a more sophisticated SAR inversion scheme for the MIZ was presented, which yields estimates for the two-dimensional ocean wave spectra in front of, and behind the sea ice boundary, as well as a two-dimensional filter function characterizing the sea ice impact on the ocean waves. The scheme makes use of first guess information taken from an ocean wave model. It was shown that the method provides results consistent with the cutoff estimation technique.

[71] It is planned to apply the above techniques on a statistical basis using complex wave mode data acquired by the ENVISAT satellite launched on March 1, 2002. The ENVISAT ASAR will provide images of 10×5 km size every 100 km along the track and thus allows to study wave damping by sea ice on a continuous basis.

[72] A statistical analysis will provide more detailed information on the wave damping mechanism and its dependence on sea ice type. In particular, this will allow to develop techniques for the estimation of classical sea ice parameters, like ice thickness or ice concentration, which are needed for the validation and assimilation of sea ice models.

[73] **Acknowledgments.** The authors would like to thank ESA for providing ERS-1/2 scenes in the framework of AO project AO2-D-146/5. The study was sponsored by the German Ministry of Education, Science, and Technology (BMBF) in the framework of the ENVOC project. The ocean wave model data were kindly provided by the European Centre for Medium-Range Weather Forecasts (ECMWF).

References

Alpers, W. R., and C. Brüning, On the relative importance of motion-related contributions to the SAR imaging mechanism of ocean surface waves, *IEEE Trans. Geosci. Remote Sens.*, *24*, 873–885, 1986.
Alpers, W. R., D. B. Ross, and C. L. Rufenach, On the detectability of ocean surface waves by real and synthetic aperture radar, *J. Geophys. Res.*, *86*, 6481–6498, 1981.
Apel, J. R., *Principles of Ocean Physics*, Academic, San Diego, Calif., 1995.
Bao, M., C. Brüning, and W. Alpers, A generalized nonlinear ocean wave SAR spectral integral transform and its application to ERS-1 SAR ocean wave imaging, in *Proceedings of the Second ERS1 Symposium on Space at the Service of our Environment, Hamburg, ESA SP-361*, pp. 219–224, Eur. Space Agency, Paris, France, 1993.
Bjorgo, E., O. M. Johannessen, and M. W. Miles, Analysis of merged SMMR-SSMI time series of Arctic and Antarctic sea ice parameters 1978–1995, *Geophys. Res. Lett.*, *24*, 413–416, 1997.
Brüning, C., W. Alpers, and K. Hasselmann, Monte-Carlo simulation studies of the nonlinear imaging of a two dimensional surface wave field by a synthetic aperture radar, *Int. J. Remote Sens.*, *11*, 1695–1727, 1990.
Carande, R. E., Estimating ocean coherence time using dual-baseline interferometric synthetic aperture radar, *IEEE Trans. Geosci. Remote Sens.*, *32*, 846–854, 1994.
Engen, G., and H. Johnson, SAR-ocean wave inversion using image cross spectra, *IEEE Trans. Geosci. Remote Sens.*, *33*, 1047–1056, 1995.
Hartmann, D. M. G., *Global Physical Climatology*, Academic, San Diego, Calif., 1994.
Hasselmann, K., Directional wave spectra observed during JONSWAP, *J. Phys. Oceanogr.*, *10*, 1264–1280, 1973.
Hasselmann, K., and S. Hasselmann, On the nonlinear mapping of an ocean wave spectrum into a synthetic aperture radar image spectrum, *J. Geophys. Res.*, *96*, 10,713–10,729, 1991.
Hasselmann, D. E., M. Dunckel, and J. A. Ewing, Directional wave spectra observed during JONSWAP 1973, *J. Phys. Oceanogr.*, *10*, 1264–1280, 1980.
Hasselmann, K., R. K. Raney, W. J. Plant, W. Alpers, R. A. Shuchman, D. R. Lyzenga, C. L. Rufenach, and M. J. Tucker, Theory of synthetic aperture radar ocean imaging: A MARSEN view, *J. Geophys. Res*, *90*, 4659–4686, 1985.
Hasselmann, S., C. Brüning, K. Hasselmann, and P. Heimbach, An improved algorithm for the retrieval of ocean wave spectra from synthetic aperture radar image spectra, *J. Geophys. Res.*, *101*, 16,615–16,629, 1996.
Horstmann, J., S. Lehner, W. Koch, and R. Tonboe, Computation of wind vectors over the ocean using spaceborne synthetic aperture radar, *Johns Hopkins APL Tech. Dig.*, *21*, 100–107, 2000.

Johannessen, O. M., S. Sandven, K. Kloster, M. Miles, V. Melentyev, and L. Bobylev, A sea ice monitoring system for the northern sea route using ERS-1 SAR data, *Tech. Rep. 103*, Nansen Environ. and Remote Sens. Cent., Bergen, Norway, 1995.
Kasilingam, D. P., and O. H. Shemdin, Models for synthetic aperture radar imaging of the ocean: A comparison, *J. Geophys. Res.*, *95*, 16,263–16,276, 1990.
Kerbaol, V., B. Chapron, and P. W. Vachon, Analysis of ERS-1/2 synthetic aperture radar wave mode imagettes, *J. Geophys. Res.*, *103*, 7833–7846, 1998.
Krogstad, H., A simple derivation of Hasselmann's nonlinear ocean–synthetic aperture radar transform, *J. Geophys. Res.*, *97*, 873–885, 1992.
Krogstad, H., O. Samset, and P. W. Vachon, Generalizations of the nonlinear ocean-SAR transformation and a simplified SAR inversion algorithm, *Atmos. Ocean*, *32*, 61–82, 1994.
Lehner, S., J. Horstmann, W. Koch, and W. Rosenthal, Mesoscale wind measurements using recalibrated ERS SAR images, *J. Geophys. Res.*, *103*, 7847–7856, 1998.
Liu, A. K., B. Holt, and P. W. Vachon, Wave propagation in the marginal ice zone: model predictions and comparisons with buoy and synthetic aperture radar, *J. Geophys. Res.*, *96*, 4605–4621, 1991a.
Liu, A. K., P. W. Vachon, and C. Y. Peng, Observation of wave refraction at the ice edge by synthetic aperture radar, *J. Geophys. Res.*, *96*, 4803–4808, 1991b.
Lyzenga, D. R., An analytic representation of the synthetic aperture radar image spectrum for ocean waves, *J. Geophys. Res*, *93*, 13,859–13,865, 1988.
Lyzenga, D. R., R. A. Shuchman, and J. D. Lyden, SAR imaging of waves in water and ice: Evidence for velocity bunching, *J. Geophys. Res.*, *90*, 1031–1036, 1985.
Mastenbroek, C., and C. F. de Valk, A semi-parametric algorithm to retrieve ocean wave spectra from synthetic aperture radar, *J. Geophys. Res.*, *105*, 3497–3516, 2000.
Shuchman, R. A., and C. L. Rufenach, Extraction of marginal ice zone thickness using gravity wave imagery, *J. Geophys. Res.*, *99*, 901–918, 1994.
Spellucci, P., *Numerische Verfahren der Nichtlinearen Optimierung*, Birkhäuser Boston, Cambridge, Mass, 1993.
Squire, V. A., J. P. Dugan, P. Wadhams, P. J. Rottier, and A. K. Liu, Of ocean waves and sea ice, *Annu. Rev. Fluid Mech.*, *27*, 115–168, 1995.
Vachon, P. W., and H. E. Krogstad, Airborne and spaceborne synthetic aperture radar observations of ocean waves, *Atmos. Ocean*, *32*, 83–112, 1994.
Vachon, P. W., R. B. Olsen, H. E. Krogstad, and A. K. Liu, Airborne synthetic aperture radar observations and simulations for waves in ice, *J. Geophys. Res.*, *98*, 16,411–16,425, 1993.
Vachon, P. W., J. C. C. Bjerkelund, F. Dobson, and M. Rey, Ship detection by the RADARSAT SAR: Validation of detection model predections, *Can. J. Remote Sens.*, *23*, 48–59, 1997.
Wadhams, P., *Ice in the Ocean*, Gordon and Breach, Newark, N. J., 2000.
Wadhams, P., and B. Holt, Waves in frazil and pancake ice and their detection in SEASAT synthetic aperture radar imagery, *J. Geophys. Res.*, *96*, 8835–8852, 1991.
Wadhams, P., V. A. Squire, D. J. Goodman, A. M. Cowan, and S. C. Moore, The attenuation rates of ocean waves in the marginal ice zone, *J. Geophys. Res.*, *93*, 6799–6818, 1988.

S. Lehner and J. Schulz-Stellenfleth, German Aerospace Center, Remote Sensing Technology Institute, Oberpfaffenhofen, D-82234 Wessling, Germany. (susanne.lehner@dlr.de; johannes.schulz-stellenfleth@dlr.de)